AGU PUBLICATIONS

JGR

Journal of Geophysical Research: Atmospheres

RESEARCH ARTICLE
10.1002/2013JD021038

Key Points:
- Most GCMs consider cloud radiation with suspended cloud
- We characterize the radiation impacts of falling snow in a CGCM
- The impacts associated with the exclusion of snow radiation are significant

Correspondence to:
J.-L. F. Li,
Juilin.F.Li@jpl.nasa.gov

Citation:
Li, J.-L. F., W.-L. Lee, D. E. Waliser, J. D. Neelin, J. P. Stachnik, and T. Lee (2014), Cloud-precipitation-radiation-dynamics interaction in global climate models: A snow and radiation interaction sensitivity experiment, *J. Geophys. Res. Atmos.*, *119*, doi:10.1002/2013JD021038.

Received 13 OCT 2013
Accepted 5 MAR 2014
Accepted article online 11 MAR 2014

Cloud-precipitation-radiation-dynamics interaction in global climate models: A snow and radiation interaction sensitivity experiment

J.-L. F. Li[1], W.-L. Lee[2], D. E. Waliser[1], J. David Neelin[3], Justin P. Stachnik[1], and Tong Lee[1]

[1]Jet Propulsion Laboratory, California Institute of Technology, Pasadena, California, USA, [2]RCEC, Academia Sinica, Taiwan, [3]Department of Atmospheric and Oceanic Sciences, University of California, Los Angeles, California, USA

Abstract Conventional global climate models (GCMs) often consider radiation interactions only with small-particle/suspended cloud mass, ignoring large-particle/falling and convective core cloud mass. We characterize the radiation and atmospheric circulation impacts of frozen precipitating hydrometeors (i.e., snow), using the National Center for Atmospheric Research coupled GCM, by conducting sensitivity experiments that turn off the radiation interaction with snow. The changes associated with the exclusion of precipitating hydrometeors exhibit a number differences consistent with biases in CMIP3 and CMIP5 (Coupled Model Intercomparison Project Phase 3 and Phase 5), including more outgoing longwave flux at the top of atmosphere and downward shortwave flux at the surface in the heavily precipitating regions. Neglecting the radiation interaction of snow increases the net radiative cooling near the cloud top with the resulting increased instability triggering more convection in the heavily precipitating regions of the tropics. In addition, the increased differential vertical heating leads to a weakening of the low-level mean flow and an apparent low-level eastward advection from the warm pool resulting in moisture convergence south of the Intertropical Convergence Zone and north of the South Pacific Convergence Zone (SPCZ). This westerly bias, with effective warm and moist air transport, might be a contributing factor in the model's northeastward overextension of the SPCZ and the concomitant changes in sea surface temperatures, upward motion, and precipitation. Broader dynamical impacts include a stronger local meridional overturning circulation over the middle and east Pacific and commensurate changes in low and upper level winds, large-scale ascending motion, with a notable similarity to the systematic bias in this region in CMIP5 upper level zonal winds.

1. Introduction

Representing atmospheric convection, precipitating/nonprecipitating clouds, their multiscale organization, and their radiation interaction in coupled atmospheric-ocean global climate models (GCMs) remains a pressing challenge to reduce and quantify uncertainties associated with present climate and climate change projections [*Stephens*, 2005; *Randall et al*., 2007]. Clouds, convection, and their radiative properties play important roles in determining global climate and weather forecast modeling and often enhance the dynamical response from latent heating alone [e.g., *Hartmann et al*., 1984; *Schumacher et al*., 2004; *W. Li et al*., 2013]. In particular, clouds control the radiative energy balance and cloud radiation feedbacks operate by trapping longwave (LW) radiation and reemitting this energy toward the surface, in addition to reflecting shortwave (SW) radiation toward the top of atmosphere (TOA). These processes and their corresponding energy balances are critical for constraining climate models and understanding the Earth's climate system [*Stephens*, 2005].

In order to accurately depict the energy and radiation balance at the surface and TOA, GCMs often represent bulk cloud properties including fractional cloud coverage and cloud hydrometeor particle size distributions and mass. In particular, the latter two quantities have been largely unconstrained in GCMs given the lack of useful observations and further quantification of their vertical structure remains a pressing challenge for remote sensing data [e.g., *Hogan et al*., 2001; *Waliser et al*., 2009, 2011; *J. L. Li et al*., 2012, 2013]. For example, *J. L. Li et al*. [2012, 2013] demonstrated that there is wide range of hydrometeor types including small (quasi-suspended/cloud) particles, large (falling/precipitating) particles, as well as convective core cloud ice, etc., that compose the cloud ice water content (CIWC) values exhibited in most of the coupled global climate models (CGCMs) contributing to Phases 3 and 5 of the Coupled Model Intercomparison Project (CMIP3 and CMIP5).

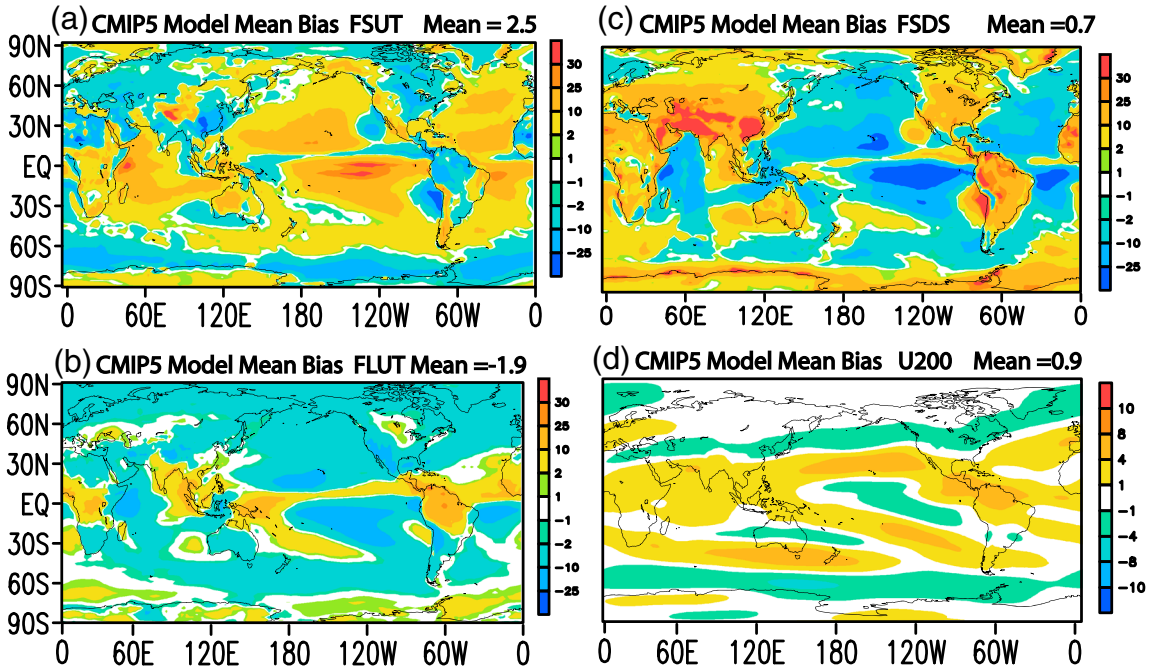

Figure 1. The annual mean maps of radiation flux bias (W m^{-2}) from the twentieth century (1970–2005) CMIP5 GCM multimodel mean (MMM) for (a) flux of radiative shortwave upward at the top of the atmosphere (FSUT); (b) flux of longwave upward at the top of atmosphere (FLUT; positive is upward); and (c) flux of shortwave downward at the surface (FSDS; positive is downward) against the CERES-EBAF annual mean (2003–2010). (d) The multimodel mean (MMM) bias of the CMIP5 GCM simulations (1970–2005) of the annual mean zonal wind at 200 hPa against the ECMWF Interim (1980–2005). Wind unit is in m s^{-1}.

The CIWC profiles derived from CloudSat [*Austin et al*., 2009], using tropospheric vertically resolved cloud radar reflectivity, when combined with data from Cloud Aerosol Lidar and Infrared Pathfinder Satellite Observations (CALIPSO) [*Delanoë and Hogan*, 2008, 2010; *Deng et al*., 2010, 2013], provide new constraints for the evaluation of global cloud mass properties in GCMs [e.g., *Chepfer et al*., 2008; *Bodas-Salcedo et al*., 2008, 2011; *Delanoë and Hogan*, 2008, 2010; *Waliser et al*., 2009; *Gettelman et al*., 2010; *Zhang et al*., 2010; *Chen et al*., 2011; *Delanoë et al*., 2011; *Jiang et al*., 2012; *Kay et al*., 2012; *Kodama et al*., 2012; *J. L. Li et al*., 2012, 2013]. These advances also include the necessary steps for a viable observational comparison of modeled clouds in terms of reflectively or radiance, typically done by using satellite "simulators" [e.g., *Klein and Jakob*, 1999; *Webb et al*., 2001] embedded in many GCMs.

Among the previous studies, *J. L. Li et al*. [2011, 2012, 2013] and *Waliser et al*. [2009, 2011] document that most of the conventional GCMs (e.g., CMIP3 and CMIP5 models) consider radiation interactions only with suspended cloud mass, ignoring falling and convective core cloud mass. Nevertheless, constraints on models' global radiation balance, clouds, and related quantities are made with measurements (e.g., CloudSat Radar and the Clouds and the Earth's Radiant Energy System (CERES) [*Wielicki et al*., 1996]) sensitive to the broader range of hydrometeors that include suspended small cloud particles, precipitating hydrometeors, and convective core mass [*Li et al*., 2011, 2012; *Waliser et al*., 2009]. Thus, most of the GCMs in CMIP3 and CMIP5 are likely to either contain significant error and/or incorrectly partition the cloud hydrometeor populations, which may result in further biases in the cloud and radiation fields [*J. L. Li et al*., 2012, 2013].

Trenberth and Fasullo [2009] provided evidence of a systematic bias in the CMIP3 radiation fields including an overestimate of the absorbed SW and outgoing LW that was most notable over heavy precipitation regions including the warm pool, midlatitudes storm tracks, and Intertropical Convergence Zone (ITCZ). *Waliser et al*. [2011] conducted a similar observation-based modeling study, leading to the hypothesis that ignoring the radiation interaction of falling snow in a model might contribute toward at least a portion of this systematic bias. This has been further supported by *J. L. Li et al*. [2013], who found the same persistent systematic biases in CMIP3 and CMIP5 (compared to observations), noting that these biases occur in conjunction with a significant underestimation of the ice water path (IWP) [see *J. L. Li et al*., 2013, Figure 13].

Figures 1a–1c reproduce the CMIP5 radiation budget biases presented in *J. L. Li et al*. [2013]. The bias patterns indicate too much TOA LW and surface SW radiation (Figures 1b and 1c, respectively) with less reflected SW

radiation at TOA (Figure 1a) in those areas with significant cloud cover and strongly precipitating/convective regions (i.e., warm pool, ITCZ, South Pacific Convergence Zone (SPCZ), Northern Hemisphere storm tracks, southern oceans, and tropical continental regions). These systematic biases can exceed 5–10 W m^{-2} both in outgoing LW radiation at the TOA and downwelling SW at the surface in the warm pool, ITCZ, and South Pacific Convergence Zone (SPCZ). Given the systemic and large-scale nature of these radiative forcing biases, we would also expect biases to be evident in the atmospheric circulation. Figure 1d shows the long-term annual multimodel ensemble mean (MMM) 200 hPa zonal wind bias from the 15 CMIP5 models [see *J. L. Li et al*., 2013, Table 3a, (1)–(15)] against the European Center for Medium-Range Weather Forecasts (ECMWF) Interim Reanalysis [*Dee and Uppala*, 2009]. The CMIP5 MMM exhibits a substantial bias with magnitudes that can be up to 6–10 m s^{-1} stronger for the subtropical (~30°N/S) eastward zonal wind (positive difference from ECMWF Interim) in the middle and east Pacific Ocean in each hemisphere, with stronger easterly zonal winds in the tropics (green shaded; negative differences from ECMWF Interim). In the Southern Ocean, the CMIP5 MMM shows weaker westerly zonal winds than in the reanalyses. One of the main considerations of this study is to explore whether aspects of the zonal wind biases, particularly near 30°N and 30°S in the middle and eastern Pacific, might be in part linked to the systematic biases on radiation shown in Figures 1a–1c, especially those differences in the deep tropics. This consideration arises in part from the study of *Waliser et al*. [2011] that illustrated sizeable biases in the radiative heating profiles, particularly at upper levels, in regions of heavy convection and precipitation when radiation interactions with precipitating hydrometeors are ignored. Such heating profile biases are likely to impact the circulation.

The purpose of this study is to extend the above work in order to quantify the systematic biases in the dynamics of the coupled ocean-atmosphere system that result from the common practice of ignoring radiative interactions with large/falling hydrometeors—in this case snow. For this purpose, we use the National Center for Atmospheric Research (NCAR) Community Earth System Model version 1 (CESM1) with Community Atmosphere Model version 5 (CAM5),a fully coupled model, to conduct several sensitivity experiments by turning on and off the radiation interaction with large-particle ice mass (i.e., snow). Specifically, we focus on the changes in the SW and LW downward fluxes at the surface (hereafter FSDS and FLDS, respectively) and upward fluxes at the TOA (hereafter FSUT and FLUT), vertical structure in radiative heating, condensational heating, as well as sea surface temperatures (SSTs), winds at 1000 hPa and 200 hPa, in addition to the local atmospheric meridional overturning circulation along the central and eastern sections of the Pacific Ocean's ITCZ.

In section 2, we briefly describe the NCAR CESM1-CAM5 coupled model including the sensitivity tests for different scenarios when omitting the frozen precipitating hydrometeors from the radiation calculations. In section 3, we illustrate and discuss the results of our model evaluation. Section 4 summarizes and draws conclusions.

2. NCAR CESM1 Coupled Model and Sensitivity Experiments

The CESM1 is a coupled climate model for simulating the Earth's climate system. Composed of four separate models that simultaneously simulate the Earth's atmosphere, ocean, land surface, and sea ice, and one central coupler component, the CESM allows researchers to conduct fundamental research into the Earth's past, present, and future climate states (model code and documentation available from http://www.cesm.ucar.edu/models/cesm1.0/). This study uses the most recent release of the NCAR CESM1 and contains options of the Community Atmosphere Model version 5 (CAM5) [*Neale et al*., 2011], Community Land Model version 4 (CLM4), the Parallel Ocean Program version 2 (POP2), as well as a slab ocean. The CAM5 physics account for and include cloud microphysics, radiative transfer, macrophysics, aerosol formation, ice clouds, and shallow convection, in addition to a new moist turbulence parameterization. Details of the performance of the cloud-related physical parameterizations can be found in *Kay et al*. [2012] and *Lindvall et al*. [2013], among other references.

The CAM5 is one of the few CMIP coupled GCMs, out of about 30, including the version 3 of the Geophysical Fluid Dynamics Laboratory Atmosphere Model [*Donner et al*., 2011], National Aeronautics and Space Administration (NASA) Goddard Earth Observing System Model, Version 5 [*Molod et al*., 2012], and NASA Goddard Institute for Space Studies model [*Schmidt et al*., 2006] that consider diagnostic falling/large-particle snow and its radiation interaction [*Kay et al*., 2012]. Snow in the model represents falling large ice crystals with appreciable fall velocities that are diagnosed from falling ice flux profiles at each model level

at each model physical time step. The model uses the four-class (liquid, ice, rain, and snow), two-moment, stratiform cloud microphysics scheme described by *Morrison and Gettelman* [2008] and also accounts for diagnosed snow mass. Snow is included in the radiation code [*Gettelman et al*., 2010], using the diagnosed mass and effective radius of falling snow crystals [*Morrison and Gettelman*, 2008]. The simulated ice and snow are comparable against CloudSat-retrieved products [*Waliser et al*., 2009; *Li et al*., 2012]. The snow particle shape recipe was based on the crystal shape observations at −45°C: 7% hexagonal columns, 50% bullet rosettes, and 43% irregular ice particles. Simulated cloud forcing and climate are sensitive to different formulations of the ice microphysics. Arctic surface radiative fluxes are sensitive to the parameterization of ice clouds. These results indicate that ice clouds including snow are potentially an important part of understanding cloud forcing and potential cloud feedbacks, particularly in the Arctic. More complete information regarding the diagnosed snow mass is described in *Morrison and Gettelman* [2008] and their radiation properties in CAM5 are provided in *Gettelman et al*. [2010]. Because it incorporates the impact of snow on radiative fluxes, CAM5 is atypical and is more consistent with observations and thus suitable for the objectives of this study [*Gettelman et al*., 2010; *Kay et al*., 2012; *J. L. Li et al*., 2012, 2013]. Note that, however, the snow radiative effects remain as an open subject needed for future investigations. For example, the diagnostic snow may bring uncertainty in snow concentrations, and it is ultimately desirable to have prognostic treatments allowing for snow to vary over time. The diagnostic snow is for stratiform grid-scale clouds while the subgrid-scale convective "floating" cloud ice and liquid are diagnosed and used for radiative transfer in a very simple form; the convective snow, however, is not yet included in NCAR CAM5 (A. Gettelman, personal communication, 2013). Diagnostic rain and associated radiation interactions have not been included in most recent version of the CAM5 model at the time of this study.

In order to explore and characterize the potential impacts of ignoring precipitating hydrometeors (i.e., snow) on radiation and the atmospheric circulation, we use the fully coupled NCAR CESM1-POP2 model with full ocean dynamics (POP2-OGCM) and conduct one sensitivity experiment by turning off the radiation interaction with snow. That is, the experiments include one simulation without diagnostic snow-radiation interaction (hereafter NoS) and the other including diagnostic snow-radiation interaction (hereafter, S). The specific experimental scenario used in the sensitivity experiment is the CMIP5 historical twentieth century simulation (1850 to 2005) initialized with the conditions from the NCAR CMIP5 "PiControl" 300 year run, which uses observed twentieth century greenhouse gas, ozone, aerosol, and solar forcing [*Taylor et al*., 2012]. The simulation time period used in the analyses presented here is 1970–2005. For both the GCM and observational data sets, all fields have been regridded and mapped onto common 2° latitude by 2° longitude grids.

3. Results

3.1. Impacts on Radiation Budget

Figure 2 shows the annual mean map of total vertically integrated cloud fraction from snow-radiation interaction on and the differences of the annual mean FSDS, FSUT, and FLUT from snow-radiation interaction off (NoS) minus snow-radiation interaction on (S) for the NCAR CESM1 sensitivity experiment (i.e., NoS − S). Figure 2 indicates that there is generally less reflected SW at TOA (Figure 2b, FSUT), more LW emission out to space at TOA (Figure 2c, FLUT), and more downward SW radiation at the surface (Figure 2d, FSDS), particularly in the areas with high cloud fraction (Figure 2a) when excluding the influence of precipitating and/or convective core hydrometeors on radiation. These effects are particularly apparent over the strongly precipitating and/or convectively active regions (e.g., midlatitudes storm tracks, warm pool, Pacific ITCZ, SPCZ, Southern Ocean, and tropical land mass over South America). These are nontrivial, systematic differences in the annual mean with values up to ~10–15 W m^{-2}, depending on the variable. The global area average of the long-term mean net total radiative flux balance is −0.17 W m^{-2} and 0.12 W m^{-2} at the TOA for the NoS and S cases, respectively. The FSUT global area mean value is 98 W m^{-2} and 100.2 W m^{-2} for the NoS and S cases, respectively, with FLUT global area mean values of 240.3 W m^{-2} and 237.8 W m^{-2}. The corresponding FSUT bias is −1.6 W m^{-2} for NoS and 0.6 W m^{-2} for S and the FLUT bias is 0.6 W m^{-2} for NoS and −1.9 W m^{-2} for S. In both simulations, the time series of global annual mean net radiative energy balanced at the TOA is within 0.7 W m^{-2}.

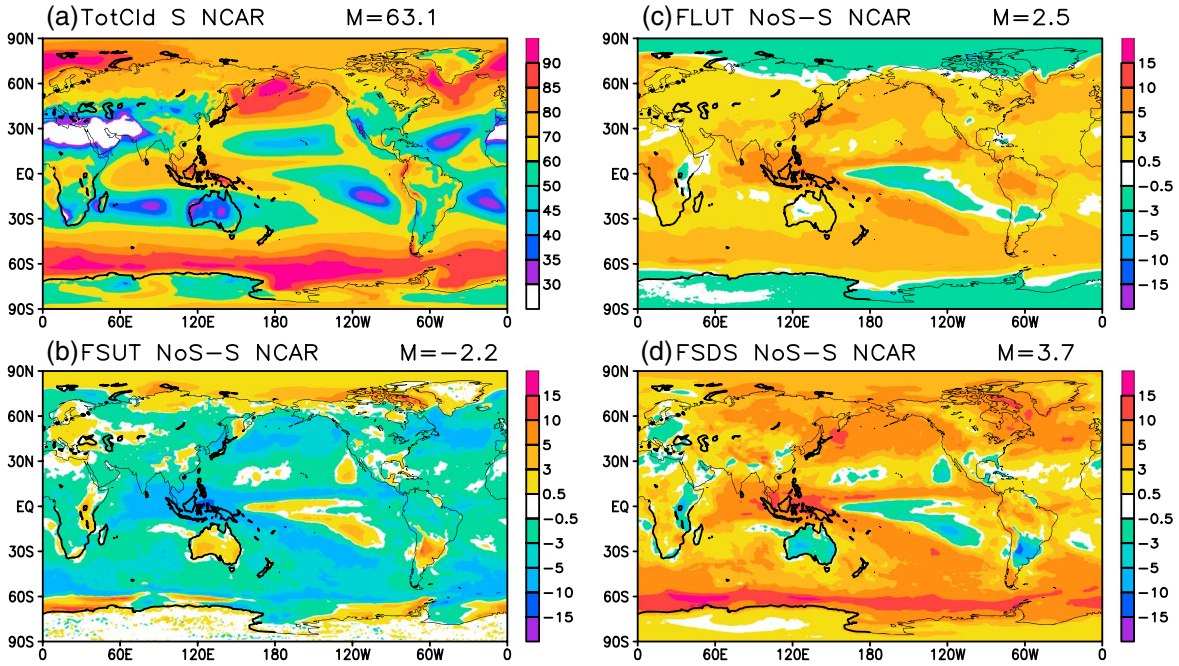

Figure 2. (a) The annual mean map of total cloud fraction (%). The changes (snow-radiative effect off (NoS) minus snow-radiative effect on (S)) of annual mean maps of (b) flux of radiative shortwave upward at the top of the atmosphere (FSUT; W m^{-2}); (c) flux of longwave upward at the top of atmosphere (FLUT; W m^{-2}); and (d) flux of shortwave downward at the surface (FSDS; W m^{-2}) from the twentieth century (1970–2005) simulations using NCAR CESM1-CAM5-POP2 for the CMIP5 historical run.

The above result is consistent with the standalone radiation model sensitivity test in *Waliser et al*. [2009] and the persistent systematic biases exhibited in CMIP3 and CMIP5 as described by *J. L. Li et al*. [2013]. Differences in the radiative fluxes are generally small over the subtropics (for both land and ocean) where the large-scale subsidence associated with the downward branch of the Hadley cell prevents most clouds from reaching the freezing level and containing significant ice mass. Notable are the regions north of SPCZ and south of the ITCZ in the equatorial central and east Pacific, which have weak radiative flux differences (up to ~5 W m^{-2}) with values of the opposite sign (i.e., an increase in FSUT and decrease in FLUT and FSDS) when excluding snow in the radiation calculations. The reasons for this less than obvious behavior appear to result from coupled dynamical interactions and are discussed in section 3.3. To develop a more thorough understanding of the nature of the above differences illustrated in Figure 2, we choose to focus on the central Pacific (60°S–60°N; 120°E–60°W) that includes strongly convective and precipitating regions over the warm pool, ITCZ, and SPCZ. This choice is based on the following: (1) the impacts on the radiative fluxes are strong, appear well defined, and appear to be closely related to the background state; (2) there is a relatively good understanding of the principle dynamical coupled processes/feedbacks in central Pacific region due to significant study of the El Niño/Southern Oscillation and other variability in this region [e.g., *Waliser et al*., 1994; *Dijkstra and Neelin*, 1995; *Munnich and Neelin*, 2004]; and (3) it lacks the additional complexities from coupling to land surfaces. Analysis focused on other regions will be reported in future papers.

Figure 3 shows the differences in annual mean surface flux quantities, precipitation, and SST from the NoS minus S simulations. Figure 3a indicates that there is generally more net downward flux of radiation, mainly contributed from the downward SW (Figure 2d), particularly in the regions of deep convection (e.g., warm pool, ITCZ, and SPCZ). The differences in precipitation rates (Figures 3a–3c, purple and black contours) show increased precipitation in the NoS case. Note that the NoS case has the same location and shape of the maximum precipitation rates as that in the S case, suggesting the differences in the model simulations might be attributed to the enhancement of precipitation rates and not a shift in the location or broadening of the maximum precipitation zones. The maximum enhanced precipitation values reach upward of 0.6 mm d^{-1} and are found over the warm pool, northeastern edge of SPCZ, and southern edge of the ITCZ (discussed further in section 3.3). Figure 3b also indicates that enhanced upward latent heat fluxes in the NoS case are found over roughly the same general regions (although not necessarily colocated with the precipitation

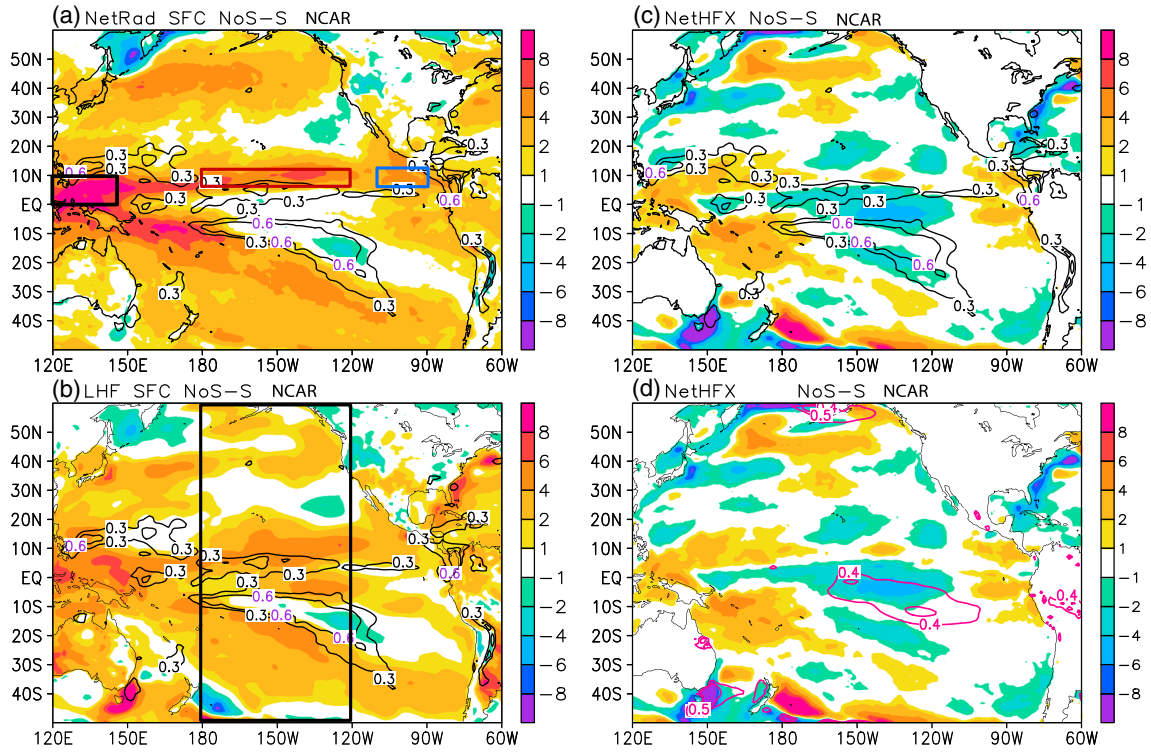

Figure 3. The changes (snow-radiative effect off minus snow-radiative effect on) of annual mean maps of (a) net flux of radiation at the surface (NetRad SFC; positive for upward flux at surface, unit: W m^{-2}); (b) same as in Figure 3a but for flux of latent heat flux at the surface (LHF SFC; positive for upward at the surface, unit: W m^{-2}); (c and d) same as in Figure 3a but for net heat at the surface (NetHFX; positive for downward flux at the surface, unit: W m^{-2}) from the twentieth century (1970–2005) simulations using NCAR CESM1-CAM5-POP2 for the CMIP5 historical run. The changes (snow-radiative effect off minus snow-radiative effect on) of the precipitation rates (contours; mm d^{-1}) are plotted in Figures 3a–3c as well as SSTs (pink color; K) in Figure 3d for reference. The colored boxes in Figure 3a are the regions used for the averaged radiative heating rate profiles in Figure 4.

changes) with excessive downward net flux of radiation. The resulting differences in net downward total heat fluxes (Figures 3c and 3d) are positive over the SPCZ and warm pool regions and negative south of the ITCZ and northeast of the SPCZ. The SSTs also increase in the NoS case in this same region between the ITCZ and SPCZ with differences up to 0.4 K (Figure 3d, pink contour) despite the negative difference in net surface heat flux in this region (Figure 3c). This feature will be discussed in section 3.3 in conjunction with the enhanced upward latent heat fluxes. Note that the SST changes are not colocated with the precipitation changes.

3.2. Impacts on Vertical Structure of Radiation and Moist Process

Figure 4 shows the shortwave (SW), longwave (LW), and the net radiative heating profile differences for NoS-S for regions over warm pool (Figure 3a, black box), eastern Pacific ITCZ (Figure 3a, blue box), and Pacific ITCZ (Figure 3a, brown box). The vertical structure of the difference profiles in each region indicates that the cooling/heating profile from the NoS case produces a temperature tendency that would yield more thermodynamically unstable columns (i.e., optically thinner clouds with SW warming below and LW cooling at midlevels and aloft near the cloud top). It is evident that there is a sizeable impact on the vertical profiles of net radiative heating dominated by LW radiative heating, with about 10–15% more cooling with respect to the mean LW radiative heating (not shown) at middle and upper tropospheric levels near the cloud top over the warm pool region (Figure 4a) and over the eastern Pacific ITCZ (Figure 4b). Similar patterns are also seen over the central Pacific ITCZ (180–120°W; 5–15°N) in Figure 4c. These results are similar to those from the standalone radiation model experiments performed in *Waliser et al.* [2011]. The compensating moist condensational heating associated with the net radiative cooling can be up to values of 0.28 K d^{-1}, for example, in the Pacific ITCZ (not shown). We note that the atmospheric dynamical response to the heating tendency will involve adjustment of the temperature profile at large scales set by wave dynamics and a response by the convective heating at smaller scales [e.g., *Emanuel et al.*, 1994].

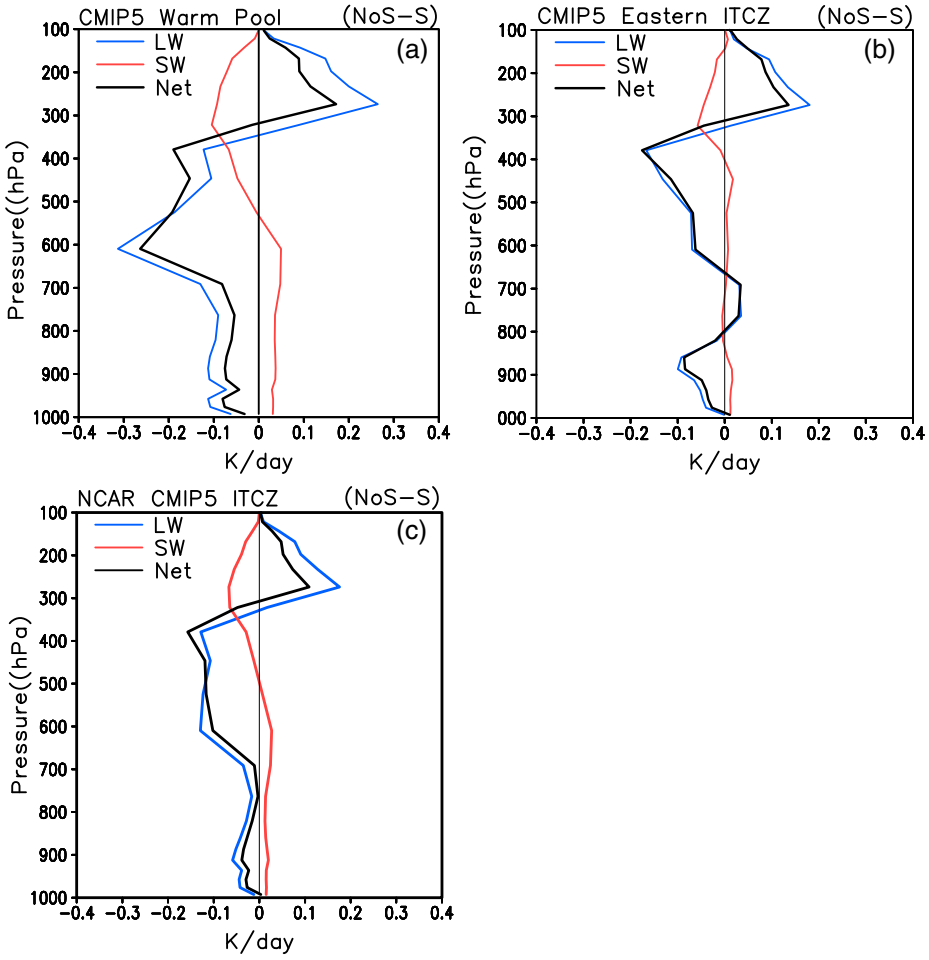

Figure 4. Annual mean differences between a case excluding effects of precipitating snow (NoS) on radiation and the control (S) for (a) shortwave radiative heating rates (red), longwave heating rate (blue) and the net heating (black) in the warm pool region (0°–10°N; 120°E–140°E) taken from the black box shown in Figure 3a. (b) The same as in Figure 4a but taken from the blue box region in the eastern Pacific (110°W–90°W; 5°N–15°N). (c) The same as in Figure 4a but taken from the brown box region in the Pacific ITCZ (5°N–15°N; 180–120°W).

In this study, we intend to characterize and understand the cloud-precipitation-radiation-dynamics interactions in the Pacific ITCZ and SPCZ where the ocean and atmosphere are closely linked through thermodynamic and dynamical processes. Figures 5a–5c show the differences in the NoS minus S simulations for the zonally averaged LW, SW, and net radiative heating rates in terms of K d^{-1} across the central and eastern Pacific ITCZ (from 180°W to 120°W; i.e., the black box in Figure 3b). These regional zonal averages are convenient for examining north-south relationships, while bearing in mind that the anomalies associated with the changes at the northeastern edge of the SPCZ, occurring at an angle relative to the equator, may be diminished and slightly smoothed. They are consistent with the upper level net radiative cooling differences associated with the exclusion of snow hydrometeors, maximizing near 600 hPa for the warm pool region (Figure 4a) and at 400 hPa for the eastern Pacific ITCZ (Figure 4b). The net heating shown in Figure 5c mainly comprises the LW cooling (QLW; Figure 5a) while the contribution from SW heating is small (QSW; Figure 5b). There is LW radiative greenhouse warming below 600 hPa in the tropical zone (~15°S to ~5°N; Figure 5a) that appears to be a result of an increase in total precipitable water through moisture convergence from the warm pool transporting moisture to the east (discussed in section 3.3). This vertical destabilizing radiative gradient associated with the exclusion of snow-radiation interaction triggers compensating deep convective updrafts resulting in stronger moist diabatic condensational heating between 5°S and 5°N with maximum heating at 400 hPa (Figure 5d). This heating difference maximum occurs slightly south of the equator, at the latitude of the southern branch of the model's double ITCZ (e.g., Figure 2a). The enhanced condensational heating (can

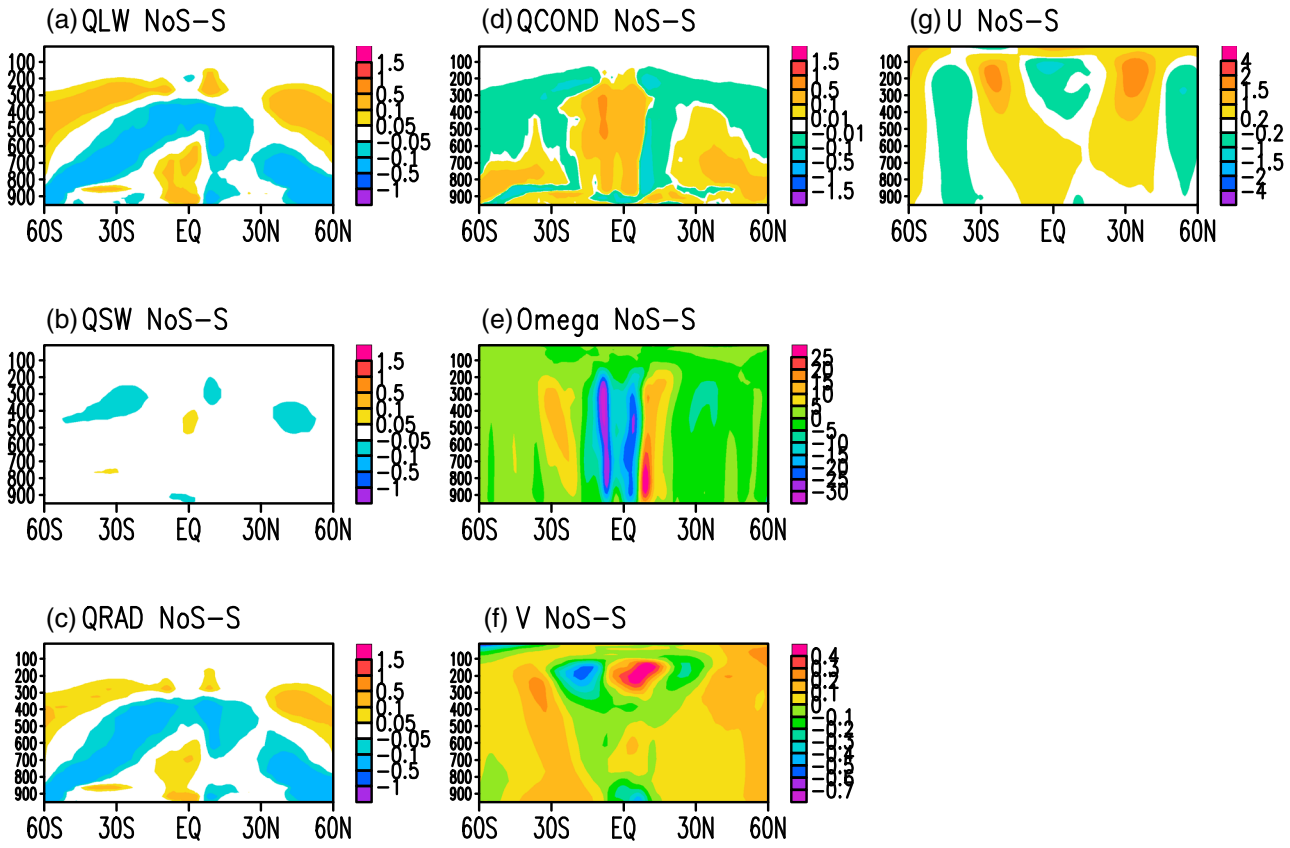

Figure 5. Annual mean changes (snow-radiation off minus snow-radiation on) for the zonal average (the black box in Figure 3b; from 180°W to 120°W; 60°S to 60°N) (a) vertical longwave (LW) heating rates (QLW; K d^{-1}); (b) shortwave heating (QSW; K d^{-1}); (c) net radiative heating rates (QRAD; K d^{-1}); (d) moist diabatic heating rates (QCOND; K d^{-1}); (e) vertical velocity (Omega; hPa h^{-1}); (f) meridional wind (V; m s^{-1}); and (g) zonal wind (U; m s^{-1}).

be up to 1 K d^{-1}) leads to a stronger vertical ascending motion (Figure 5e) in the north and south branches of the ITCZ (~10°S and ~5°N) with maximum differences near 400 hPa. Figure 5f also indicates greater low-level meridional convergence and upper level divergence shown as well as upper level subtropical westerly jets and slight easterly enhancements in the tropics (Figure 5g).

3.3. Impacts on Dynamics in Middle and Eastern Tropical Pacific

The stronger local large-scale ascending motions shown in Figure 5e and corresponding map of the vertical velocity at 500 hPa (Figure 6a), associated with neglecting snow-radiation interactions, imply local low-level wind convergence (Figure 6b) over the northern edge of the SPCZ and slightly south of the ITCZ in accordance with the regions of greatest increase in precipitation rate (contours). Although the mean low-level flow continues to be easterly in each case, there is also greater apparent moisture and warm air advection along the belt of 5°N–10°S and 150°E–120°W (Figure 6b) originating from the warm pool (i.e., weaker transport of relatively cold and dry air owing to the westerly wind differences between the models) resulting in more moist and warmer air and enhanced precipitation (contours) into the V-shaped regions between Pacific ITCZ and SPCZ (Figure 6c). This weakening of the mean flow and effective enhancement in the low-level eastward/southeastward wind is potentially a contributing factor in warmer SSTs (Figure 6d) between the Pacific ITCZ and SPCZ due to the effect of wind stress changes on ocean dynamics, keeping in mind that the net surface heat flux (Figure 3d), which would be needed to balance the changes in ocean heat convergence, is not large. Another potential effect on SST is that the wind anomalies represent a reduction in the strength of the trade winds in the southeastern Pacific, i.e., in the V-shaped regions between Pacific ITCZ and SPCZ. This would tend to reduce evaporation, leading to SST increasing. Note that the maximum enhanced precipitation rates are found over the maximum low-level wind convergence (i.e., maximum vertical velocity shown in Figure 6a) rather than over warmest SSTs (Figure 6d). These mechanisms (i.e., eastward and southeastward moist and

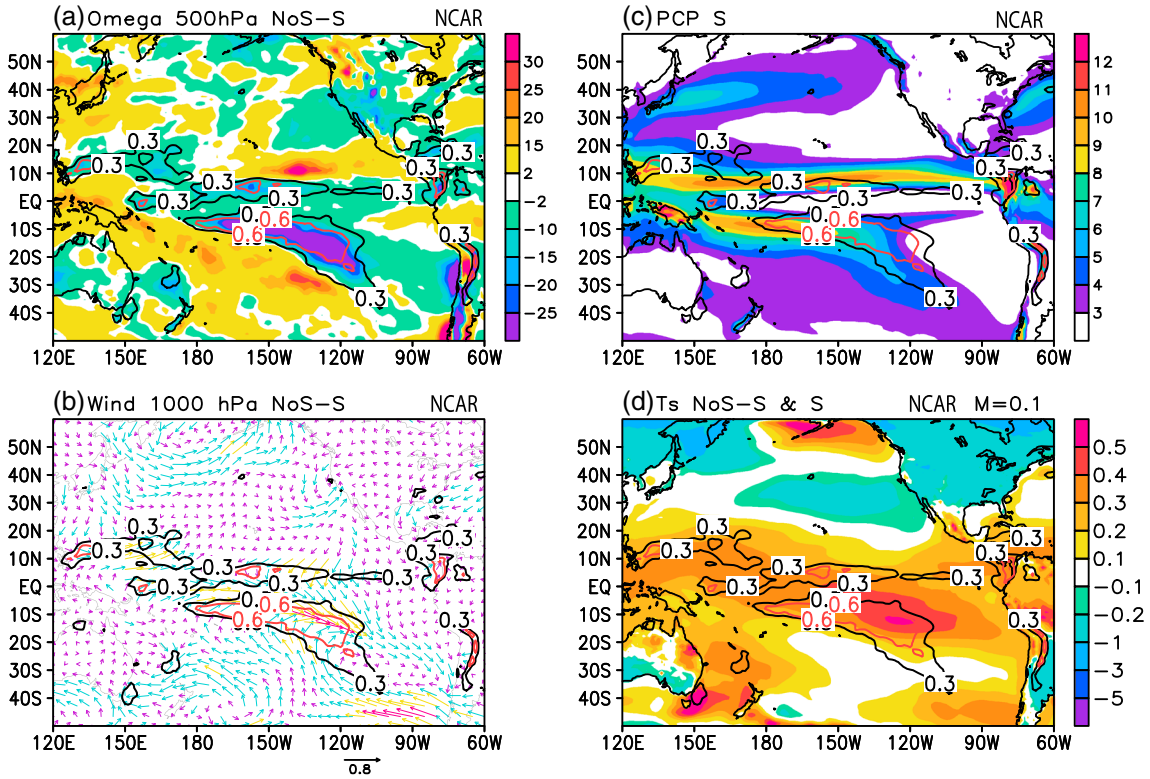

Figure 6. The changes (snow-radiative effect off minus snow-radiative effect on) of annual mean maps of (a) vertical upward motion at 500 hPa (Omega; negative for upward motion, unit: Pa h^{-1}) with the changes of the precipitation rates (color contours; mm d^{-1}); (b) same as in Figure 6a but for wind vector changes at the 1000 hPa (Wind; unit: m s^{-1}); (c) same as in Figure 6a but for the annual mean map of total precipitation rates (PCP; mm d^{-1}) for snow-radiative effect on; and (d) same as in Figure 6a but for the changes of annual mean surface temperatures (Ts; unit: K) from the twentieth century (1970–2005) simulations using NCAR CESM1-CAM5-POP2 for the CMIP5 historical run.

warmer air advections from the warm pool) associated with neglecting the snow radiation appear to have substantial impacts on the mean northwestward dry/cold air advection from the cold SSTs regions off the coast of the Peru into the regions shown in Figure 7a. This is potentially consistent with insufficient dry air transport from the southeast being a contributing factor in the overextension of the SPCZ [*Lintner and Neelin*, 2008] and the concomitant excess in precipitation occurring along the northern edge of the SPCZ (Figure 6c). The lack of dry air transport and overextension of the SPCZ may in turn be responsible for warmer SSTs (Figure 6d) and the greater total precipitable water (up to 2 mm) shown in Figure 7b (black contour) in the NoS case. These precipitable water anomalies tend to be collocated with the regions of enhanced precipitation (red contours) illustrated in Figure 7b, which is also consistent with the changes in moisture advection that appear to contribute to precipitation changes in these regions as discussed above.

3.4. Impacts on Dynamics in Subtropical Pacific

Figure 8a shows the changes (NoS − S) of annual mean maps of cloud condensational heating rates at 500 hPa (triggered in part by the radiative-driven column destabilizing tendency shown in Figure 4) indicating more condensational heating over the warm pool and ITCZ (equator to 10°N and 150°E–150°W) and the southern edge of the model's SPCZ near 120°W and 20°S. This asymmetric difference in tropical heating induces an atmospheric dynamical response with an asymmetric spatial pattern change about the equator in the zonal westerlies (~2.5 m s^{-1}). The peak NoS − S differences occur to the east of the jet stream (Figure 8b) in the Northern Hemisphere at 35°N and in the Southern Hemisphere near 30°S [e.g., *Wallace et al.*, 1998]. In addition, there is upper level easterly wind acceleration (i.e., negative difference) in the deep tropics along the equator. It should be noted that the differences (NoS − S) in the wind fields at 200 hPa occur at a significant level close to 98% and above using a standard *t* test (not shown). Geopotential changes (not shown) tend to be spread out over a Rossby radius of deformation by equatorial

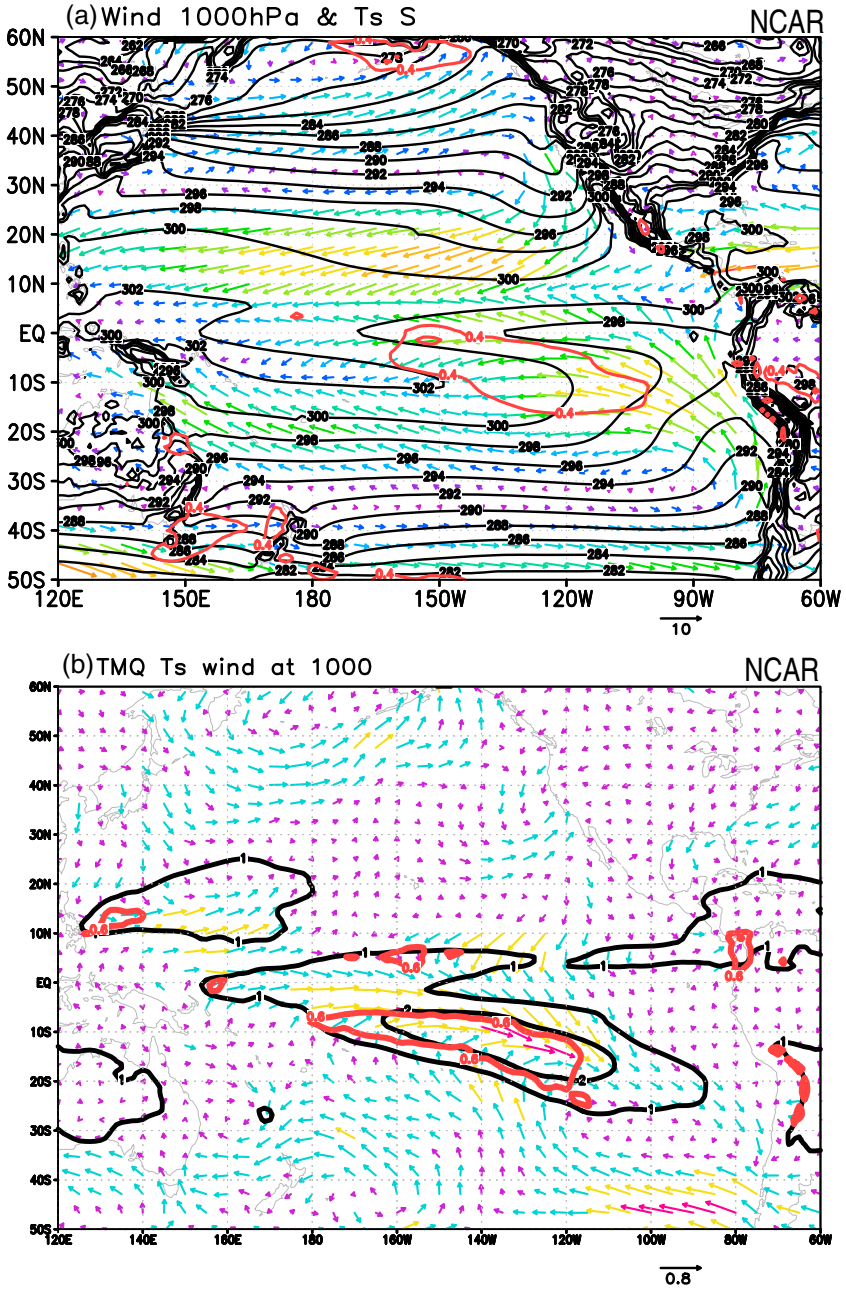

Figure 7. (a) The annual mean map of sea surface temperature (thick solid black contour; K) from the snow-radiative effect on simulation and the annual mean wind vectors at 1000 hPa (color wind vectors; m s^{-1}). The changes (snow-radiative effect off minus snow-radiative effect on) of annual mean surface temperatures are contoured for values equal to and greater than the value of 0.4 K from the twentieth century (1970–2005) simulations using NCAR CESM1-CAM5-POP2 for the CMIP5 historical run. (b) The changes (snow-radiative effect off minus snow-radiative effect on) of the annual mean map of total (vertically integrated) precipitable water (TMQ; solid black contour greater than 1 mm or kg m^{-2}), and precipitation rate changes of values equal to and greater than 0.6 mm d^{-1} (thick red contours). Vectors indicate changes of annual mean 1000 hPa winds (m s^{-1}) from the twentieth century (1970–2005) simulations using NCAR CESM1-CAM5-POP2 for the CMIP5 historical run.

wave dynamics. This upper level asymmetric zonal wind change is consistent with the NoS − S differences in the meridional overturning circulations in the mid-to-east Pacific Ocean, where there is enhanced regional zonal-average meridional winds (180°W to 120°W; Figure 5f) and stronger zonal winds at upper levels along 30°N and 25°S (Figure 5g).

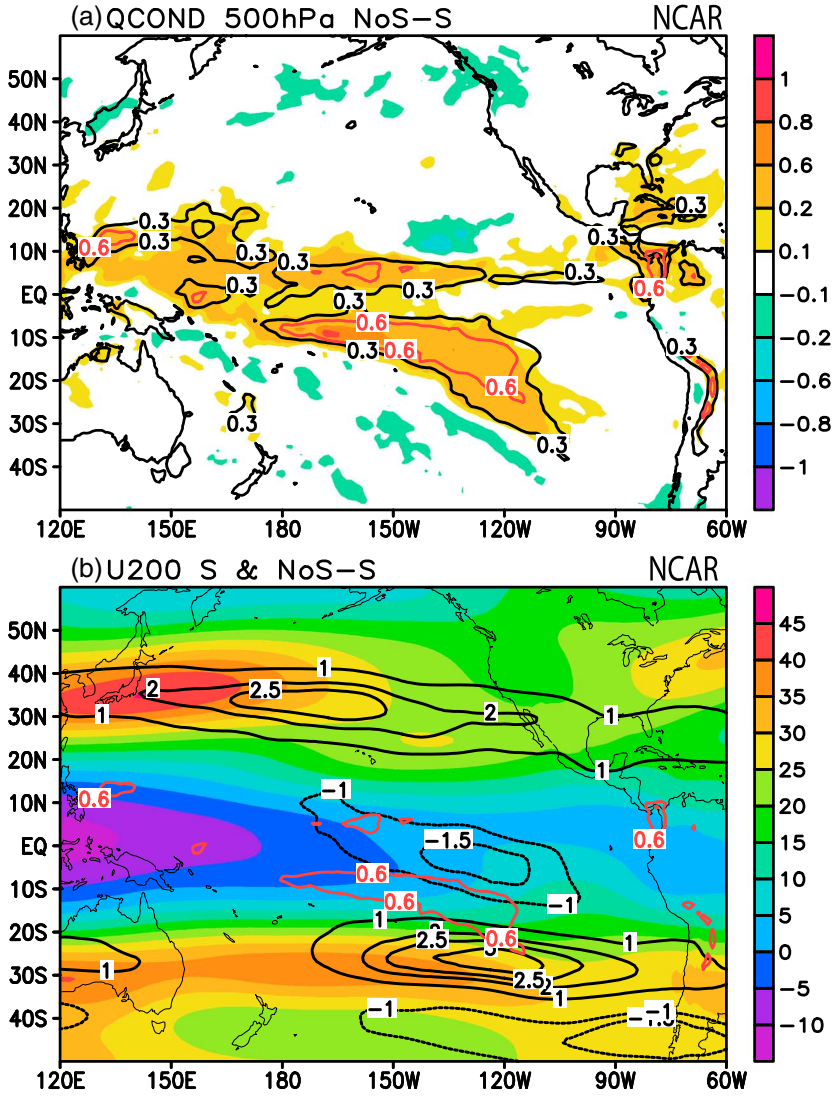

Figure 8. (a) The changes (snow-radiative effect off minus snow-radiative effect on) of annual mean maps of cloud condensational heating rates at 500 hPa (QCOND; thick color contours, K d^{-1}). (b) The annual mean map of zonal wind velocity at 200 hPa with the snow-radiation interaction on (shaded color; U200; m s^{-1}) and the changes (snow-radiative effect off minus snow-radiative effect on) of zonal wind at 200 hPa (thick black contour: m s^{-1}). Red contours in both panels indicate regions with precipitation rate changes greater than 0.6 mm d^{-1} from the twentieth century (1970–2005) simulations using NCAR CESM1-CAM5-POP2 for the CMIP5 historical run.

3.5. Impacts on Dynamics Compared to CMIP5 Simulation Bias

Figure 9 compares 200 hPa zonal wind differences (NoS − S) from the present experiments with the 200 hPa zonal wind biases in the multimodel mean for CMIP5. There is considerable similarity in the spatial distribution of the NoS − S zonal wind differences at 200 hPa (between 50°S and 60°N) shown in Figure 9a and the long-term annual mean zonal wind biases from the multimodel mean (MMM) CMIP5 simulations, relative to the ECMWF Interim Reanalysis (Figure 9b). Note that the magnitudes of the subtropical westerly zonal wind bias (~30°) from the CMIP5 MMM can be up to 6–10 m s^{-1} (positive difference from ECMWF Interim) in the middle and east Pacific Ocean in each hemisphere, with a weaker but still sizeable near-equatorial easterly zonal wind bias (green/blue shaded; negative differences from ECMWF Interim). While the patterns exhibit a striking similarity, it is noted that magnitude of the NoS − S peak differences is about 40% of the size of the peak biases in CMIP5.The spatial correlation from the NoS − S CAM5 sensitivity test and CMIP5 zonal wind bias at 200 hPa is mildly high with a value of 0.72. The CAM5 bias of the 200 hPa zonal

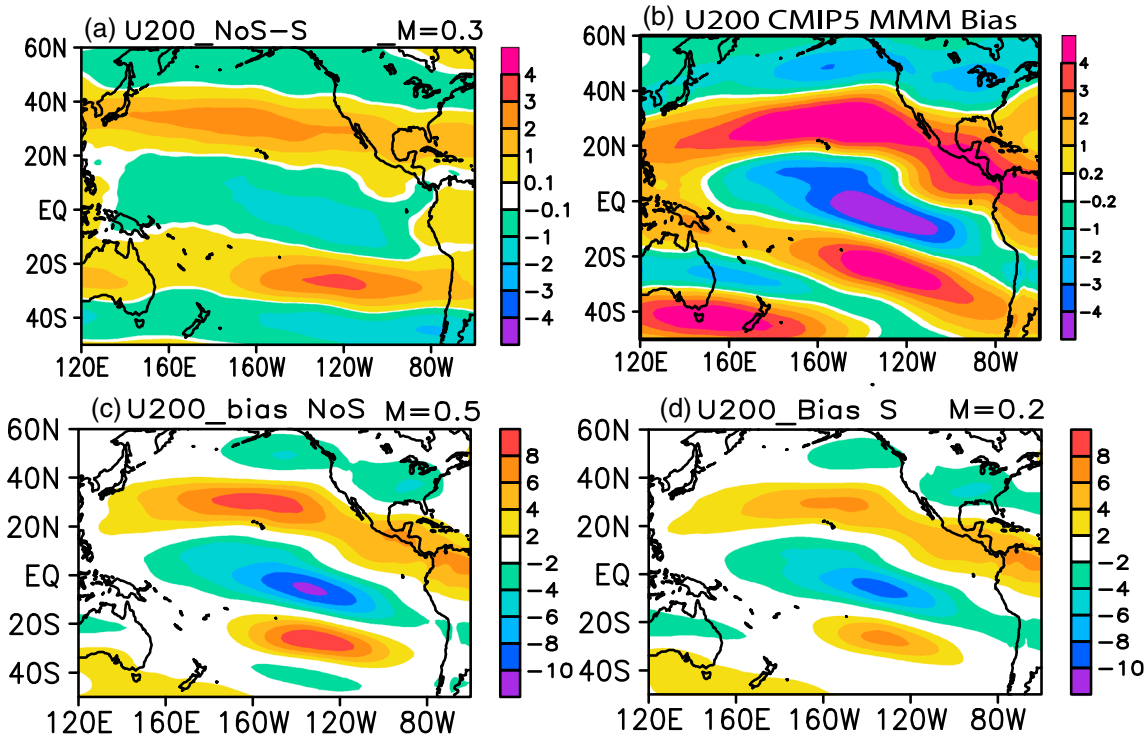

Figure 9. Annual mean changes (snow-radiation off minus snow-radiation on) for (a) zonal wind at 200 hPa (m/s) from NCAR CESM1 sensitivity experiments; (b) the bias of the CMIP5 GCM simulations multimodel mean (MMM) of zonal wind at 200 hPa (m s^{-1}) from the twentieth century (1970–2005) CMIP5 GCM simulations against the ECMWF Interim annual mean (1980–2005). (c) The bias of zonal wind at 200 hPa from the snow-radiative effect off (NoS) on simulation the NCAR CMIP5 against ECMWF Interim (m/s); (d) same as Figure 9c but from snow-radiative effect on (S).

winds compared against the ECMWF Interim Reanalysis illustrates some degree of improvement (about ~50%) when transitioning from the snow-radiation interaction off (Figure 9c) to snow-radiation interaction on case (Figure 9d) in the model. These results suggest that the exclusion of the radiative effects of snow may indeed be responsible for a substantial part of the CMIP5 MMM upper level wind bias, though there may also be other contributing factors.

4. Summary and Discussion

Most GCMs represent the liquid and ice in the atmospheric column that reside in clouds but typically do not represent liquid and ice in falling particles and the convective core, such as rain and/or snow. Observationally based products, including CloudSat and CALIPSO, to first order, represent total tropospheric ice, as the measurements are sensitive to a wide range of particle sizes, including small (quasi-suspended/cloud) particles, large (falling/precipitating) particles, and convective core cloud ice. The last two particle types are generally not included as diagnostic/prognostic variables in most current GCMs [e.g., *Waliser et al*., 2009; *J. L. Li et al*., 2012, 2013]. In this paper, we explored the dynamical impacts on the zonal jets and local meridional overturning circulation in the central Pacific and those related ocean-atmosphere coupled dynamics associated with ignoring the frozen precipitating hydrometeors in the radiation calculations using fully coupled NCAR CESM1 model simulations, by turning on and off the radiation interaction with snow.

Changes in the radiation budget for the model experiments over the tropical and subtropical Pacific regions are shown in Figures 10a–10c and display many consistencies with the CMIP5 radiation budgets presented in *J. L. Li et al.* [2013] (reproduced in Figures 10d–10f). They found systematic radiation budget biases in a multimodel examination of CMIP3 and CMIP5 simulations related to a significant underestimation of the ice water path (IWP). This indicates too much TOA LW and surface SW radiation with less reflected SW radiation at TOA in the strongly precipitating/convective regions (i.e., warm pool, ITCZ, SPCZ, and Northern Hemisphere storm tracks) when excluding the influence of precipitating and convective core hydrometeors on radiation. Nontrivial systematic biases shown in Figure 10 in precipitating and convectively active regions of the tropics can be up to

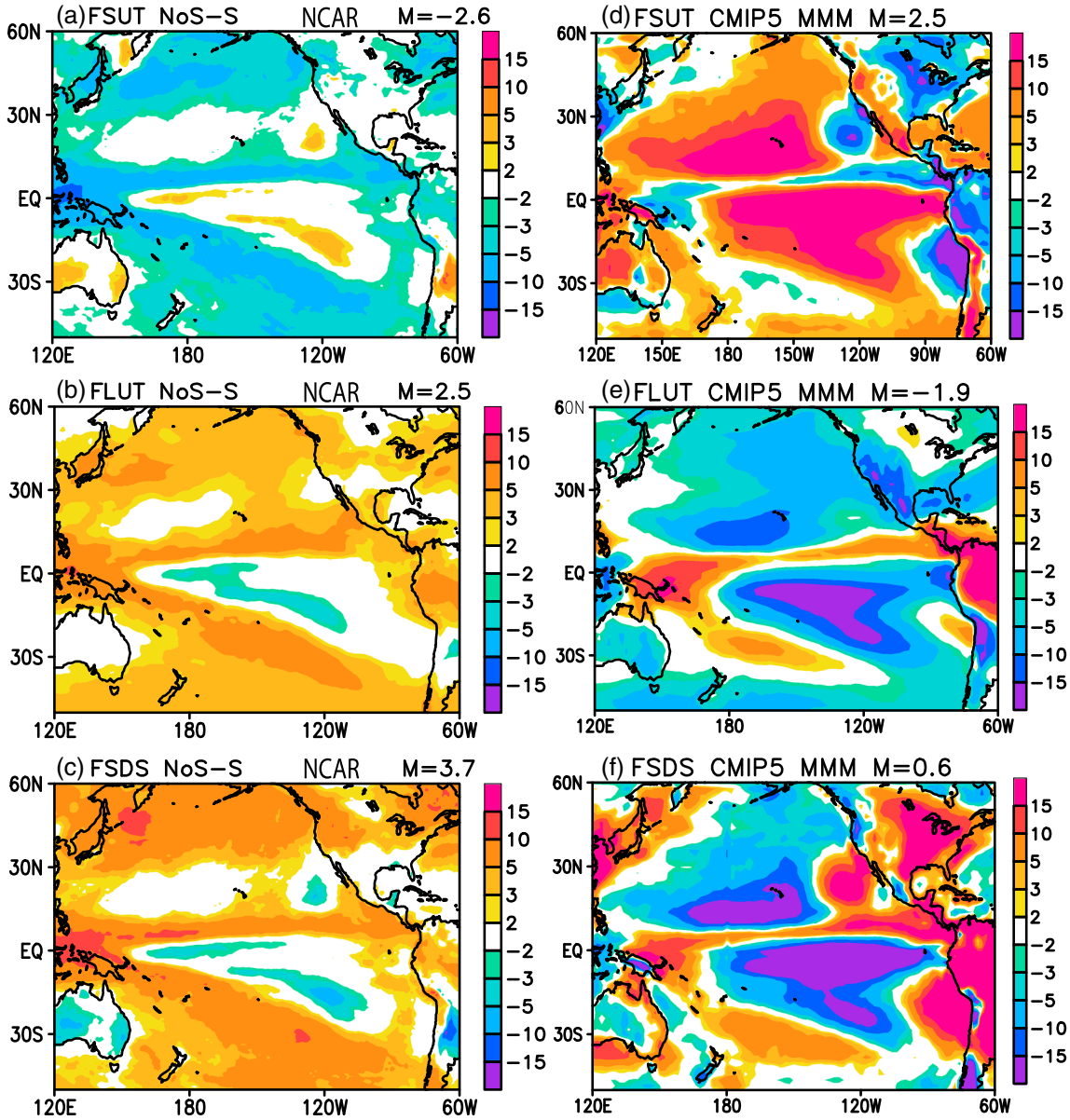

Figure 10. The changes (snow-radiative effect off (NoS) minus snow-radiative effect on (S)) of annual mean maps of (a) flux of radiative shortwave upward at the top of the atmosphere (FSUT; positive is upward); (b) flux of longwave upward at the top of atmosphere (FLUT; positive is upward); and (c) flux of shortwave downward at the surface (FSDS; positive is downward) from the twentieth century (1970–2005) simulations using NCAR CESM1-CAM5-POP2 for the CMIP5 historical run. Taken from *J. L. Li et al.* [2013] are the annual mean maps of radiation flux from the twentieth century (1970–2005) CMIP5 GCM multimodel mean (MMM) bias of (d) flux of radiative shortwave upward at the top of the atmosphere; (e) flux of longwave upward at the top of atmosphere (FLUT; positive is upward, W m^{-2}); and (f) flux of shortwave downward at the surface (FSDS; positive is downward) against the CERES-EBAF annual mean (2003–2010). All flux units are in W m^{-2}.

~5–10 W m^{-2} both in outgoing LW radiation at the TOA and downwelling SW at the surface in the eastern Pacific ITCZ [*J. L. Li et al.*, 2013]. Note that the differences between in Figures 1a–1c and 10d–10f both show large, compensating bias patterns in regions dominated by deep convection (where the NoS − S changes shown in Figures 2c and 2d are also largest) and those in other portions of the tropical ocean. The extent to which the changes in deep convective regions in the NoS − S experiments are balanced by those in other portions of the tropical oceans appears less than in the CMIP5 bias patterns.

Figure 11 shows the bias in FSDS, FLUT, and FSUT from the snow-radiative effect off (NoS) and snow-radiative effect on (S) against reference quantities from CERES-Energy Balance and Filled (EBAF) observations. The

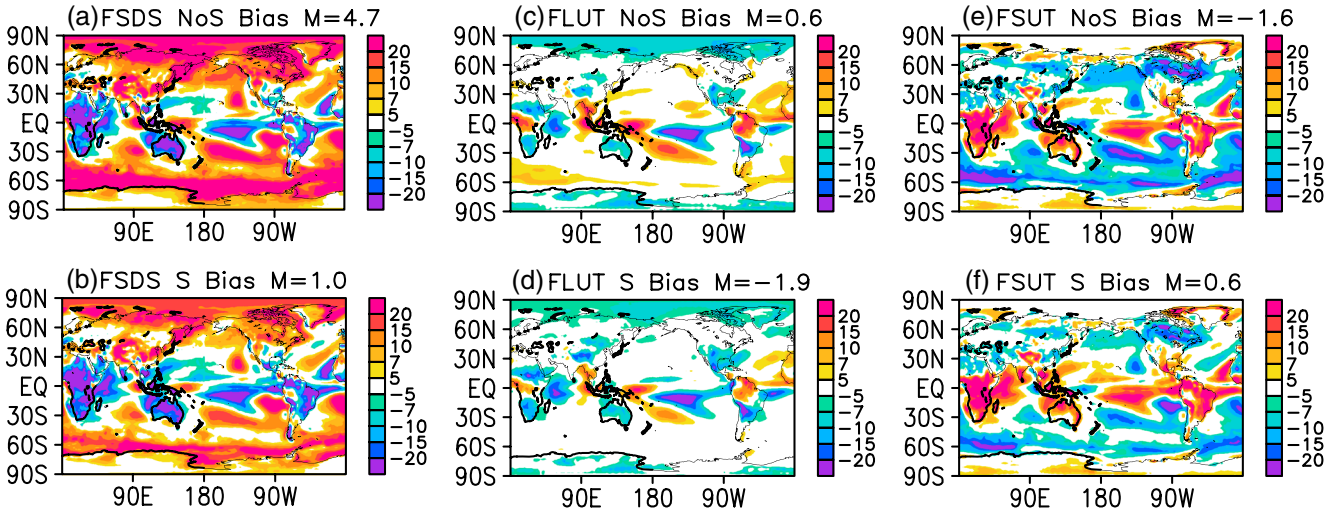

Figure 11. (a) The bias in flux of shortwave downward at the surface (FSDS; positive is downward) from the snow-radiative effect off case (NoS) against CERES-EBAF; (b) same as in Figure 11a but for snow-radiative effect on (S); (c and d) same as in Figures 11a and 11b but for flux of longwave upward at the top of atmosphere (FLUT; positive is upward); (e and f) same as in Figures 11a and 11b but for flux of radiative shortwave upward at the top of the atmosphere (FSUT; positive is upward). All flux units are in W m^{-2}.

biases of the radiative fluxes demonstrate some improvement (most notably for the FLUT) for the snow-interaction on case (i.e., smaller biases for S when compared to the NoS case) over heavy rainfall regions such as the ITCZ, warm pool, and SPCZ.

Apart from this fidelity assessment of the models' representation of radiation, we seek to investigate the dynamical impacts of ignoring the radiation interaction with precipitating and convective clouds, a common practice in most CGCMs contributing to CMIP3 and CMIP5 [*J. L. Li et al.*, 2012, 2013]. Given the sizeable radiative forcing biases due to the misrepresentation of clouds in the CGCMs, we expect equally sizeable biases related to changes in the atmospheric circulation.

The results from the fully coupled simulations using the NCAR CESM1 indicate that changes in the radiation fields (NoS − S) have some suggestive similarities in spatial pattern to the biases from most of the CGCMs and their ensemble mean in CMIP3 and CMIP5 [*J. L. Li et al.*, 2013]. While not suggesting that all of the biases in the CMIP5 models are due to the snow-radiative effect, it is a plausible contributor given that few of the models include this effect. It is thus well worth understanding how this effect plays out in terms of dynamical interactions in the set of experiments presented here.

By turning on and off snow radiative effects, the coupled simulations indicate too much TOA LW radiation and downward SW radiation at the surface (Figures 2, 3, and 10) that can be up to 15 W m^{-2} in the strongly precipitating/convective regions when excluding the influence of precipitating hydrometeors on radiation. Moreover, there is a sizeable impact on the vertical profiles of radiative heating (Figures 4, 5a, and 5c), with about 10–20% excessive cooling at middle-upper tropospheric levels near the cloud top. This vertically destabilizing radiative heating (Figure 5c) triggers compensating deep convective activity (Figure 5e) with stronger condensational heating (Figure 5d) resulting in enhanced local ascending and descending motions (Figure 5e). The vertical circulation change produces low-level wind convergence that reduces dry air advection by the southeasterly trades (i.e., anomalous southeastward advection of moist, warm air; Figure 7b) resulting in enhanced precipitation along the northeastern edge of SPCZ (Figures 6a and 6d). This mechanism can have a substantial impact on the north and eastward edge of the SPCZ, causing increased moisture and associated precipitation increases (Figure 7). This appears to partially correct biases associated with insufficient mean dry and cold air transports from the Southeast Pacific (Figure 7a), which is a potentially important contributing factor in SPCZ overextension shown in Figure 6c.

In terms of the impacts on dynamics, the results from these NCAR CESM1 sensitivity tests show that the differences in the upper level (200 hPa) winds are similar to those found in the CMIP5 ensemble average when compared to ECMWF Interim Reanalyses (Figure 9). Changes are also noted in the magnitude of the

poleward flow at upper levels in the tropics, resulting in an overall stronger meridional overturning in the central and east Pacific (e.g., Figure 5f). The changes of asymmetric upper level (200 hPa) maximum zonal wind along the equator (Figure 8b) are found to be associated with the snow-radiation interaction off at the Northern (at 40°N, 170°W) and Southern (at 30°S, 110°W) Hemispheres at the edge of maximum diabatic heating near the warm pool/ITCZ and southern tip of the SPCZ (Figure 8a), consistent with the Rossby wave dynamical response to tropical heating.

From previous work and what we have found in this study, it is suggested that the ensemble CMIP3 and CMIP5 radiative fields [*J. L. Li et al*., 2013], IWP [*Waliser et al*., 2009; *Li et al*., 2012], and dynamics show plausibly and physically consistent biases (against observational data). These results suggest the effects of including precipitating clouds and convection in a model's radiation calculations could impact other aspects of the coupled climate system, such as the atmospheric and ocean circulations in CGCMs. We suggest that it is a necessary to consider the inclusion of the precipitating and convective core hydrometeors and their radiative effects in coupled GCMs. Currently, there are models in progressing to include prognostic stratiform snow and rain for radiation calculation such as in NCAR CAM AGCM (A. Gettelman, personal communication, 2013).

Acknowledgments

We thank Akio Arakawa at UCLA, Sun Won, Qing Yue, Seungwon Lee, Eric Fetzer, and Bin Guan at JPL as well as H.-H. Hsu at Academia Sinica, Taiwan, for useful comments. This work has been supported in part by the NASA Making Earth System Data Records for Use in Research Environments (MEaSUREs) and Earth Science Data Records Uncertainty (ESDR-ERR) programs and in part by the NOAA NA11OAR4310099 (J.D.N.). The contributions by D.E.W. and J.L.L. to this study were carried out on behalf of the Jet Propulsion Laboratory, California Institute of Technology, under a contract with the National Aeronautics and Space Administration.

References

Austin, R. T., A. J. Heymsfield, and G. L. Stephens (2009), Retrieval of ice cloud microphysical parameters using the CloudSat millimeter-wave radar and temperature, *J. Geophys. Res.*, *114*, D00A23, doi:10.1029/2008JD010049.

Bodas-Salcedo, A., M. J. Webb, M. E. Brooks, M. A. Ringer, K. D. William, S. F. Milton, and D. R. Wilson (2008), Evaluating cloud systems in the Met Office global forecast model using simulated CloudSat radar reflectivities, *J. Geophys. Res.*, *113*, D00A13, doi:10.1029/2007JD009620.

Bodas-Salcedo, A., et al. (2011), COSP: Satellite simulation software for model assessment, *Bull. Am. Meteorol. Soc.*, *92*, 1023–1043, doi:10.1175/2011BAMS2856.1.

Chen, W.-T., C. P. Woods, J.-L. F. Li, D. E. Waliser, J.-D. Chern, W.-K. Tao, J. H. Jiang, and A. M. Tompkins (2011), Partitioning CloudSat ice water content for comparison with upper-tropospheric ice in global atmospheric models, *J. Geophys. Res.*, *116*, D19206, doi:10.1029/2010JD015179.

Chepfer, H., S. Bony, D. Winker, M. Chiriaco, J.-L. Dufresne, and G. Sèze (2008), Use of CALIPSO lidar observations to evaluate the cloudiness simulated by a climate model, *Geophys. Res. Lett.*, *35*, L15704, doi:10.1029/2008GL034207.

Dee, D. P., and S. Uppala (2009), Variational bias correction of satellite radiance data in the ERA-Interim reanalysis, *Q. J. R. Meteorol. Soc.*, *135*, 1830–1841, doi:10.1002/qj.493.

Delanoë, J., and R. J. Hogan (2008), A variational scheme for retrieving ice cloud properties from combined radar, lidar, and infrared radiometer, *J. Geophys. Res.*, *113*, D07204, doi:10.1029/2007JD009000.

Delanoë, J., and R. J. Hogan (2010), Combined CloudSat-CALIPSO-MODIS retrievals of the properties of ice clouds, *J. Geophys. Res.*, *115*, D00H29, doi:10.1029/2009JD012346.

Delanoë, J., R. J. Hogan, R. M. Forbes, A. Bodas-Salcedo, and T. H. M. Stein (2011), Evaluation of ice cloud representation in the ECMWF and UK Met Office models using CloudSat and CALIPSO data, *Q. J. R. Meteorol. Soc.*, *137*, 2064–2078, doi:10.1002/qj.882.

Deng, M., G. G. Mace, Z. Wang, and H. Okamoto (2010), Tropical composition, cloud and climate coupling experiment validation for cirrus cloud profiling retrieval using CloudSat radar and CALIPSO lidar, *J. Geophys. Res.*, *115*, D00J15, doi:10.1029/2009JD013104.

Deng, M., G. G. Mace, Z. Wang, and P. Lawson (2013), Evaluation of several A-Train ice cloud retrieval products with in situ measurements collected during the SPARTICUS campaign, *J. Appl. Meteorol. Climatol.*, *52*, 1014–1030.

Dijkstra, H. A., and J. D. Neelin (1995), Ocean–atmosphere interaction and the tropical climatology. Part II: Why the Pacific cold tongue is in the east, *J. Clim.*, *8*, 1343–1359.

Donner, L. J., et al. (2011), The dynamical core, physical parameterizations, and basic simulation characteristics of the atmospheric component of the GFDL coupled model CM3, *J. Clim.*, *24*, 3484–3519, doi:10.1175/2011JCLI3955.1.

Emanuel, K. A., J. D. Neelin, and C. S. Bretherton (1994), On large-scale circulations in convecting atmospheres, *Q. J. R. Meteorol. Soc.*, *120*, 1111–1143.

Gettelman, A., X. Liu, S. J. Ghan, H. Morrison, S. Park, A. J. Conley, S. A. Klein, J. Boyle, D. L. Mitchell, and J.-L. F. Li (2010), Global simulations of ice nucleation and ice supersaturation with an improved cloud scheme in the Community Atmosphere Model, *J. Geophys. Res.*, *115*, D18216, doi:10.1029/2009JD013797.

Hartmann, D. L., H. H. Hendon, and R. A. Houze Jr. (1984), Some implications of the mesoscale circulations in tropical cloud clusters for large-scale dynamics and climate, *J. Atmos. Sci.*, *41*, 113–121.

Hogan, R. J., C. Jakob, and A. J. Illingworth (2001), Comparison of ECMWF winter-season cloud fraction with radar-derived values, *J. Appl. Meteorol.*, *40*, 513–525.

Jiang, J. H., et al. (2012), Evaluation of cloud and water vapor simulations in CMIP5 climate models using NASA A-Train satellite observations, *J. Geophys. Res.*, *117*, D14105, doi:10.1029/2011JD017237.

Kay, J. E., et al. (2012), Exposing global cloud biases in the Community Atmosphere Model (CAM) using satellite observations and their corresponding instrument simulators, *J. Clim.*, *25*, 5190–5207, doi:10.1175/JCLI-D-11-00469.1.

Klein, S. A., and C. Jakob (1999), Validation and sensitivities of frontal clouds simulated by the ECMWF model, *Mon. Weather Rev.*, *127*(10), 2514–2531.

Kodama, C., A. T. Noda, and M. Satoh (2012), An assessment of the cloud signals simulated by NICAM using ISCCP, CALIPSO, and CloudSat satellite simulators, *J. Geophys. Res.*, *117*, D12210, doi:10.1029/2011JD017317.

Li, J.-L. F., D. E. Waliser, and J. H. Jiang (2011), Correction to "Comparisons of satellites liquid water estimates to ECMWF and GMAO analyses, 20th century IPCC AR4 climate simulations, and GCM simulations", *Geophys. Res. Lett.*, *38*, L24807, doi:10.1029/2011GL049956.

Li, J.-L. F., et al. (2012), An observationally-based evaluation of cloud ice water in CMIP3 and CMIP5 GCMs and contemporary analyses, *J. Geophys. Res.*, *117*, D16105, doi:10.1029/2012JD017640.

Li, J.-L. F., D. E. Waliser, G. Stephens, S. Lee, T. L'Ecuyer, S. Kato, N. Loeb, and H.-Y. Ma (2013), Characterizing and understanding radiation budget biases in CMIP3/CMIP5 GCMs, contemporary GCM, and reanalysis, *J. Geophys. Res. Atmos.*, *118*, 8166–8184, doi:10.1002/jgrd.50378.

Li, W., C. Schumacher, and S. A. McFarlane (2013), Radiative heating of the ISCCP upper level cloud regimes and its impact on the large-scale tropical circulation, *J. Geophys. Res. Atmos.*, *118*, 592–604, doi:10.1002/jgrd50114.

Lindvall, J., G. Svensson, and C. Hannay (2013), Evaluation of near-surface parameters in the two versions of the atmospheric model in CESM1 using flux station observations, *J. Clim.*, *26*, 26–44, doi:10.1175/JCLI-D-12-00020.1.

Lintner, B. R., and J. D. Neelin (2008), Eastern margin variability of the South Pacific Convergence Zone, *Geophys. Res. Lett.*, *35*, L16701, doi:10.1029/2008GL034298.

Molod, A., L. Takacs, M. Suarez, J. Bacmeister, I.-S. Song, and A. Eichmann (2012), The GEOS-5 atmospheric general circulation model: Mean climate and development from MERRA to Fortuna, Technical report series on global modeling and data assimilation, 28.

Morrison, H., and A. Gettelman (2008), A new two-moment bulk stratiform cloud microphysics scheme in the NCAR Community Atmosphere Model (CAM3), part I: Description and numerical tests, *J. Clim.*, *21*, 3642–3659.

Munnich, M., and J. D. Neelin (2004), Where is ENSO stress balanced?, *Atmos. Sci. Lett.*, *5*, 13–22.

Neale, R. B., et al. (2011), Description of the NCAR Community Atmosphere Model (CAM5), *Tech. Rep. NCAR/TN-4861STR*, 268 pp., Natl. Cent. for Atmos. Res., Boulder, Colo.

Randall, D. A., et al. (2007), Climate models and their evaluation, in *Climate Change 2007: The Physical Science Basis, Contribution of Working Group I to the Fourth Assessment Report of the Intergovernmental Panel on Climate Change*, edited by S. Solomon et al., pp. 589–662, Cambridge Univ. Press, Cambridge, U. K.

Schmidt, G. A., et al. (2006), Present day atmospheric simulations using GISS ModelE: Comparison to in-situ, satellite and reanalysis data, *J. Clim.*, *19*, 153–192.

Schumacher, C., R. A. Houze Jr., and I. Kraucunas (2004), The tropical dynamical response to latent heating estimates derived from the TRMM precipitation radar, *J. Atmos. Sci.*, *61*, 1341–1358.

Stephens, G. L. (2005), Cloud feedbacks in the climate system: A critical review, *J. Clim.*, *18*, 237–273.

Taylor, K. E., R. J. Stouffer, and G. A. Meehl (2012), An overview of CMIP5 and the experiment design, *Bull. Am. Meteorol. Soc.*, *93*, 485–498.

Trenberth, K. E., and J. T. Fasullo (2009), Simulation of present day and 21st century energy budgets of the southern oceans, *J. Clim.*, *23*, 440–454.

Waliser, D. E., B. Blanke, J. D. Neelin, and C. Gautier (1994), Shortwave feedbacks and El Niño-Southern Oscillation: Forced ocean and coupled ocean–atmosphere experiments, *J. Geophys. Res.*, *99*(C12), 25,109–25,125, doi:10.1029/94JC02297.

Waliser, D. E., et al. (2009), Cloud ice: A climate model challenge with signs and expectations of progress, *J. Geophys. Res.*, *114*, D00A21, doi:10.1029/2008JD010015.

Waliser, D. E., J.-L. F. Li, T. S. L'Ecuyer, and W.-T. Chen (2011), The impact of precipitating ice and snow on the radiation balance in global climate models, *Geophys. Res. Lett.*, *38*, L06802, doi:10.1029/2010GL046478.

Wallace, J. M., E. M. Rasmusson, T. P. Mitchell, V. E. Kousky, E. S. Sarachik, and H. vonStorch (1998), On the structure and evolution of ENSO-related climate variability in the tropical Pacific: Lessons from TOGA, *J. Geophys. Res.*, *103*(C7), 14,241–14,259, doi:10.1029/97JC02905.

Webb, M., C. Senior, S. Bony, and J. J. Morcrette (2001), Combining ERBE and ISCCP data to assess clouds in the Hadley Centre, ECMWF and LMD atmospheric climate models, *Clim. Dyn.*, *17*(12), 905–922.

Wielicki, B. A., B. R. Barkstrom, E. F. Harrison, R. B. Lee, G. L. Smith, and J. E. Cooper (1996), Clouds and the Earth's radiant energy system (CERES): An Earth observing system experiment, *Bull. Am. Meteorol. Soc.*, *77*, 853–868.

Zhang, Y., S. A. Klein, J. Boyle, and G. G. Mace (2010), Evaluation of tropical cloud and precipitation statistics of Community Atmosphere Model version 3 using CloudSat and CALIPSO data, *J. Geophys. Res.*, *115*, D12205, doi:10.1029/2009JD012006.